Guided Formation of Large Crystals of Organic and Perovskite Semiconductors by an Ultrasonicated Dispenser and Their Application as the Active Matrix of Photodetectors

Chenning Liu,[†,⊥] Hang Zhou,[‡,⊥] Qian Wu,[†] Fuhua Dai,[†] Tsz-Ki Lau,[§] Xinhui Lu,[§] Tengzhou Yang,[†] Zixin Wang,[†] Xuying Liu,[‖] and Chuan Liu*[,†]

[†]State Key Laboratory of Optoelectronic Materials and Technologies and the Guangdong Province Key Laboratory of Display Material and Technology, School of Electronics and Information Technology, Sun Yat-sen University, Guangzhou 510275, P. R. China

[‡]Shenzhen Key Lab of Thin Film Transistor and Advanced Display, Peking University Shenzhen Graduate School, Peking University, Shenzhen 518055, P. R. China

[§]Department of Physics, The Chinese University of Hong Kong, New Territories, Hong Kong, P. R. China

[‖]School of Materials Science and Engineering, Zhengzhou University, 100 Kexue Avenue, Zhongyuan, Zhengzhou 450001, Henan, P. R. China

ⓢ *Supporting Information*
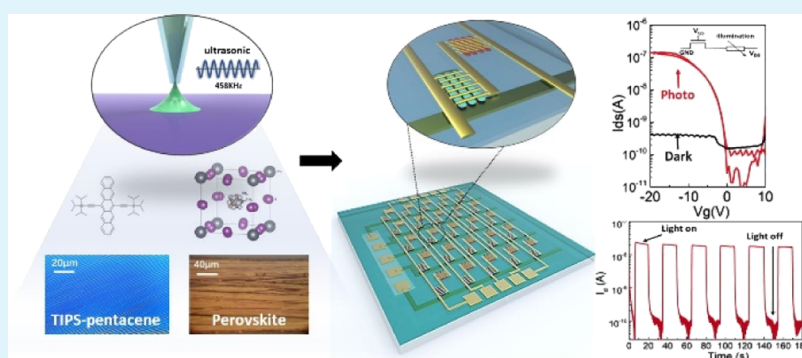
ABSTRACT: The crystallization of organic or perovskite semiconductors reflects the intermolecular interactions and crucially determines the charge transport in opto-electronic devices. In this report, we demonstrate and investigate the use of an ultrasonicated dispenser to guide the formation of crystals of organic and perovskite semiconductors. The moving speed of the dispenser affects the match between the concentration gradient and evaporation rate near the three-phase contact lines and thus the generation of various crystallization morphologies. The mechanism of crystallization is given by a relationship between the calculated concentration gradient profile and the degree of crystal alignment. Highly ordered, aligned crystals are achieved for both organic bis(triisopropylsilylethynyl)-pentacene and perovskite $MAPbI_3$ semiconductors. Absorption spectra, Raman scattering spectroscopy analysis, and grazing incidence wide-angle X-ray scattering measurement reveal the strong anisotropy of the crystalline structures. The aligned crystals lead to remarkably enhanced electrical performances in an organic thin-film transistor (OTFT) and perovskite photodetector. As a demonstration, we combine the OTFT with photodetectors to achieve an active matrix of normally off, gate-tunable photodetectors that operate under ambient conditions.

KEYWORDS: *ultrasonicated dispensing, organic semiconductor, perovskite, crystallization, transistor, photodetector*

1. INTRODUCTION

Printing electronic technologies have attracted tremendous attention for their potential use in flexible manufacturing with the competitive advantages of large area, low cost, and the capability to print various patterns for matrix or circuits, avoiding the traditional photolithography procedure and potential destruction to the films. Particularly, inkjet printing, a typical technology of direct-write printing, was first investigated and has been widely applied in electronic devices,[1,2] biological devices,[3,4] and other sensors[5,6] Never-

theless, disconnected drops of ink ejected from the nozzle under pressure could cause discontinuity of the film. Several technologies appear to improve the problem. Hasegawa et al.[7] have used a dual-head printer to generate continuous small-molecular semiconducting films under the principle of antisolvent crystallization. The Jurchescu[8] and Shkunov[9]
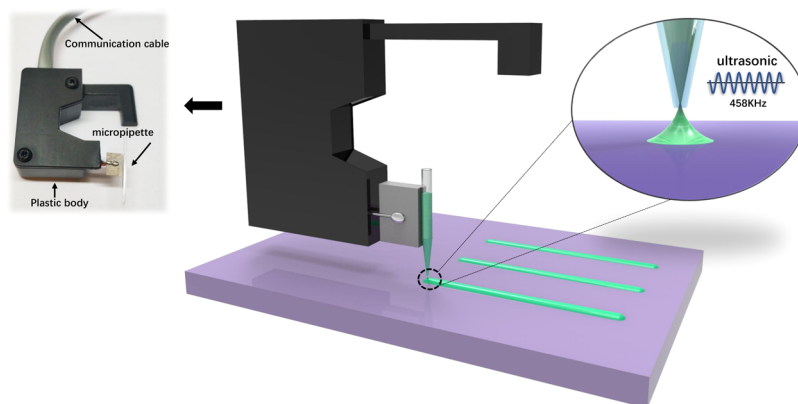
Figure 1. Ultrasonic vibrated dispenser: optical image (left) and schematic representation (right) including the micropipette, plastic body, plastic takedown screws, communication cable, and piezo.

teams have both used the spray printing method to produce uniform organic thin films, in which the ink is atomized by an external force before dispensing from the nozzle to avoid discrete droplets. In the usual noncontact, ink-jet printing, the solution droplet is released by a pulse of piezoelectric effect, drops from the nozzle, and hits the substrate (Figure S1). Solutions or inks with high viscosity or low polarity require high electric field to be printed out continuously and stably.[10−12] Also, the process of falling out of the nozzle and hitting the substrate surface needs particular optimizations on the viscosity, polarity, and other parameters of the solution.[13,14] Here, we utilize an ultrasonicated dispenser to guide the formation of crystals and obtain a tunable morphology of crystal films of organic and perovskite semiconductors, including remarkably aligned crystals with high electrical performance. Furthermore, we produce active photodetector arrays based on the organic thin-film transistor (OTFT) and a perovskite with the large-area, low-temperature direct-write printing technology.

The setup and working principle of an ultrasonicated dispenser is shown in Figure 1. The key parts of the dispenser are a quartz micropipette for holding the solution, fixed with a piezo actuator controlled by electric voltage. A plastic body connects them with a communication cable for digital control. The micropipette is loaded with solution when dipped into a solution reservoir due to the capillary force. The printing process is briefly illustrated in Figure 1 (right). As the filled micropipette gradually approaches the substrate (5 μm between tip and substrate, Figure S3), a liquid meniscus forms to connect the substrate and micropipette. On account of the inverse piezoelectric effect, the micropipette vibrates at the frequency of 458 kHz under the voltage applied by the piezo. The solution is continuously released of the needle by vibration and deposited on the substrate with the micropipette moving along a predefined path. Different from the conventional inkjet printing that delivers discrete liquid drops onto the substrate, the vibration-assisted dispensing allows the droplet to be in touch with the substrate, guarantees stably and continuously releasing of solutions, and gives a high tolerance for viscosity and polarity of solutions. The intimate contact between solution droplet and the substrate reduces the effect of viscosity and splashing.

In previous studies, the ultrasonic vibrated dispenser has been mainly employed to print metal nanoparticles or nanowires[6] for conducting electrodes or interconnects. The unique feature of the dispenser is that it bridges the liquid between the static substrate and the dynamically moving micropipette. Here, we take advantage of such a feature and investigate the remarkable capability to control the morphology and guide the crystallization of organic and perovskite semiconductors, in order to obtain well-aligned crystals and to improve electrical performance in field-effect transistors[15] and photodetectors,[16] respectively. In this study, we investigate how to control solution deposition and to guide the crystallization of the semiconductors by tuning the dynamic nature of the dispenser. After optimizing an abundance of deposition conditions (moving speed, concentration of the solution, temperature of the substrate, etc.), we study the impact of various crystallizations on the electrical performance of thin-film transistors (TFTs) and photodetectors based on these crystals. Furthermore, we demonstrate how to apply such a technique to make the active matrix of photodetectors, which exhibits superior performance compared with that of a single phototransistor or photodetector.

2. EXPERIMENTAL SECTION

2.1. Crystal Growth and Characterization. Bis-(triisopropylsilylethynyl) (TIPS)-pentacene (purchased from Sigma-Aldrich) dissolved in Anisole (purchased from Sigma-Aldrich) with different concentrations respectively is used as the printing ink. PbI$_2$ (purchased from Aldrich) was mixed with MAI on the molar mass ratio of 1:1, dissolved in DMF (10 wt %), and then heated for 3 h at temperature of 70 °C with tinfoil packaged. The solutions were printed into crystalline films by SonoPlot Microplotter II with an operation voltage of 0.1 V. Grazing incidence wide-angle X-ray scattering (GIWAXS) measurements were carried out by an Xeuss 2.0 SAXS/WAXS laboratory beamline using a Cu X-ray source (8.05 keV, 1.54 Å) and a PILATUS3 R 300K detector. The incidence angle is 0.2°. The absorption spectra were recorded by a UV−visible spectrophotometer (Thermo Scientific, Evolution 220). Polarized Raman spectroscopy was measured using a Renishaw inVia Reflex (laser spot size is 1−2 μm, 532 nm, 485 μW).

2.2. Device Fabrication. N-doped silicon with 300 nm SiO$_2$ dielectric layers is served as a substrate, which were first cleaned in an ultrasonic bath using acetone, alcohol, and deionized water. Then, the substrate was dipped in piranha solution (H$_2$SO$_4$/H$_2$O$_2$ = 3:1) to make a super-hydrophilicity surface. We then used poly-methyl methacrylate (PMMA) to modify the substrates, which improves wetting of the printed solution and thus the crystal formation and film uniformity for TIPS-pentacene (Figure S2).[17−19] PMMA (Sigma-Aldrich, M_w = 20 000) dissolved in anisole (0.5 wt %) was spin-coated with the speed of 500 rpm for 5 s and then 2000 rpm for 30 s, followed by annealing at 120 °C for 20 min. The printing was carried
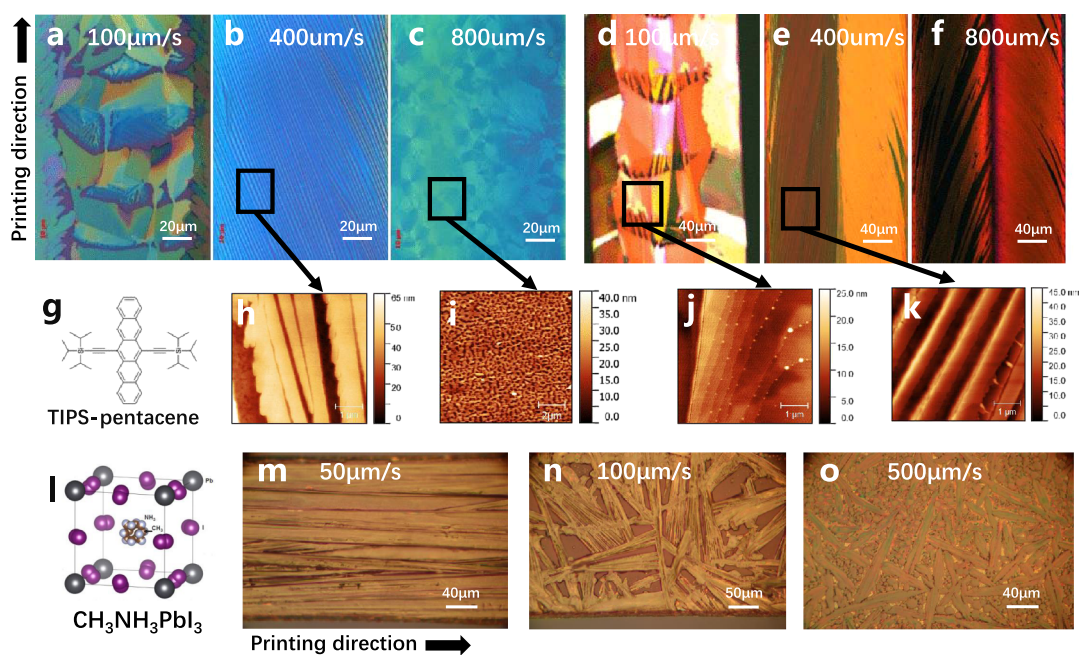
Figure 2. POM images of TIPS-pentacene crystals obtained from depositing a solution of (a−c) 0.5 wt % or (d−f) 0.6 wt % at speeds of 100, 400, and 800 μm/s. (g) Chemical structure of TIPS-pentacene. (h−k) AFM images of the films shown in (b−e). (l) Chemical structure of the perovskite. (m−o) POM images of crystals obtained from a perovskite solution of 10 wt % printed at 500, 100, and 50 μm/s.

out in ambient conditions with the substrates heated under 50 °C for TIPS-pentacene and 60 °C for perovskite. Subsequently, gold source−drain electrodes were deposited (40 nm, 0.2 Å/s) by thermal evaporation in vacuum (6×10^{-4} Pa) through shadow masks.

2.3. Device Characterization. The OTFT devices (without passivation layer) were electrically characterized by a semiconductor parameter analyzer (Agilent, B1500A) under ambient and dark conditions at room temperature. The photo-electric response of photodetectors was characterized in air by a semiconductor parameter analyzer (Agilent, B1500A) in the dark or under illumination with a white light from the microscope.

3. RESULTS AND DISCUSSION

3.1. Control of Crystal Morphology. The crystals of TIPS-pentacene printed with optimized conditions are shown in Figure 2. The size of the well-organized crystal is around several hundreds of micrometers and some reach millimeters, which is comparable with those obtained from other methods such as zone-casting,[20,21] shearing,[22] dip coating,[23] and gap casting.[24] They are also much longer and better aligned as compared with the crystals deposited by spin-coating (Figure S6a) with the spherical crystals in tens of micrometers and without orientation. This is because in spin-coating the solution evaporates quickly,[25] and the concentration gradient sharply decreases from the liquid−air interface to the solid−liquid interface.[26,27] As a result, a large number of crystallites form spontaneously from the supersaturated solution near the liquid−air interface.[28] In comparison, the micropipette of the dispenser moves at a selected speed with releasing the solution stably and continuously, which leads to a concentration gradient along the printing direction and can be tuned to match the evaporation rate.

We optimized the deposition conditions including substrate surface and temperatures (see Experimental Section) and then systematically studied how the moving speed of the micro-pipette influences the meniscus and the crystal morphology. By varying the moving speeds as 100, 400, and 800 μm/s when

depositing a 0.5 wt % solution of TIPS-pentacene, three different morphologies are obtained including small pieces of platelike crystals (thick and discontinuous, Figure 2a), thin crystalline belts along the printing direction (Figure 2b), and isotropic, spherical crystals (Figure 2c). By further employing atomic force microscopy (AFM) to reveal the micrometer-scale morphology, we observed well-aligned crystals with a uniform height at the printing speed of 400 μm/s (Figure 2h). We measured the thickness of the film in about 100−200 nm by a surface profiler (Figure S9) and observed gaps among crystals in some films by a polarized optical microscopy (POM) system (Figure S4). Especially, the films printed at a high speed of 800 μm/s exhibit spherical crystals with a large number of microscopic voids (Figure 2i), which may deteriorate the charge transport in device operations.[29,30]

The concentration of the TIPS-pentacene solution was increased from 0.5 to be 0.6 wt % to investigate the impact of the solution concentration. When setting the moving speed as 100 μm/s, similar platelike crystals were also obtained but are larger and thicker (compare Figure 2d and 2a). Especially, in the AFM characterization, lamina structures with well-defined crystal terraces are found in the platelike crystals obtained at low speeds (Figure 2j). At a speed of 400 μm/s, ribbonlike crystals appear and are slimmer and denser than those obtained at 0.5 wt % (compare Figure 2e and 2k with 2b). When the printing velocity is 800 μm/s, well-aligned crystals are still generated compared with the spherical crystals obtained at the lower concentration (compare Figure 2f and 2c). Note that there is no interchain entanglement among small molecules as occurs in polymers,[31,32] and thus, we can neglect the changes in viscosity for solutions of various concentrations.[33]

When depositing the perovskite MAPbI$_3$ solution (10 wt %) at speeds of 50, 100, and 500 μm/s, a change of morphology was also observed. The morphology changes from very uniformly aligned, crystalline belts along the printing direction
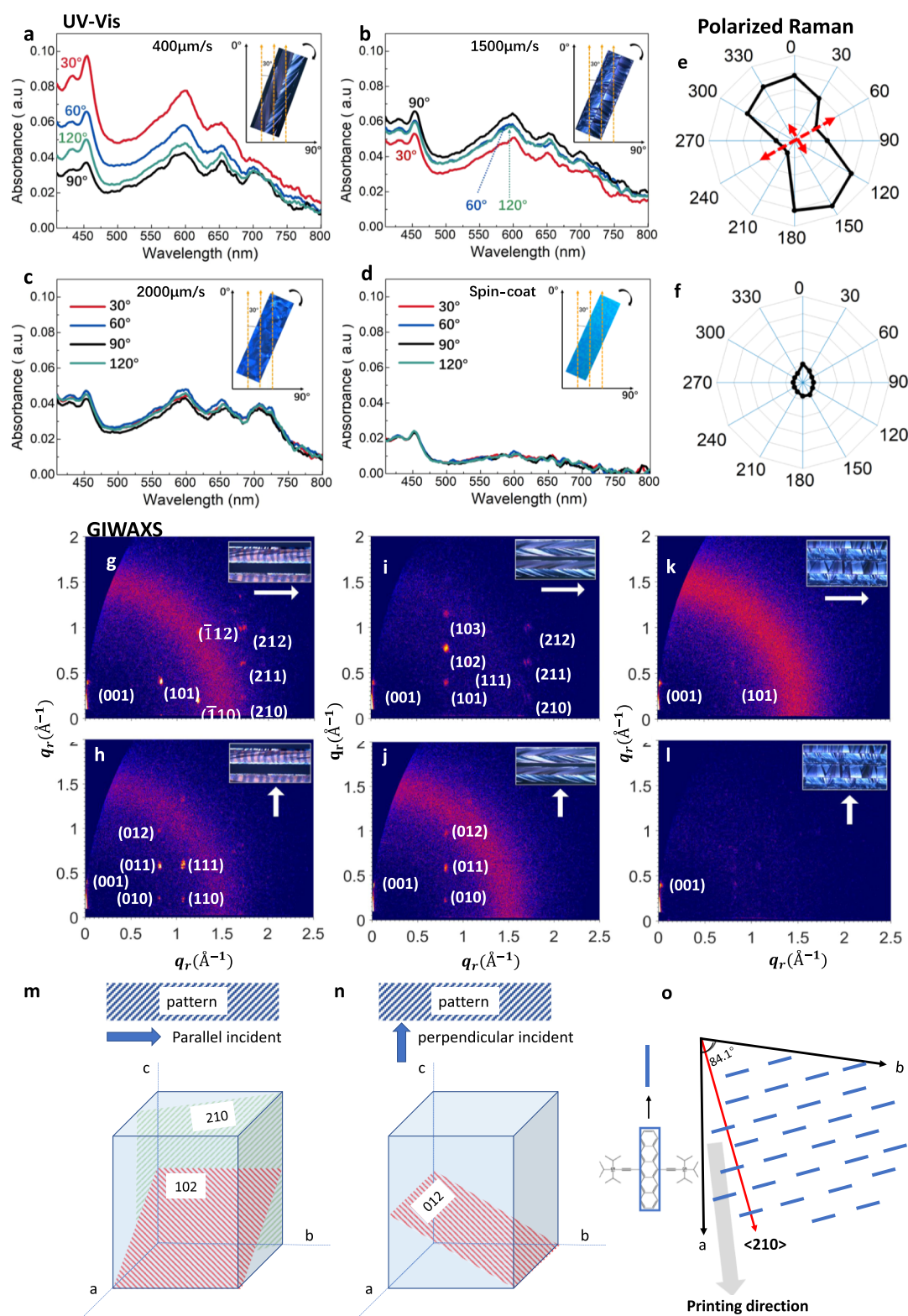
Figure 3. (a−d) UV−vis absorption spectra of TIPS-pentacene deposited at 400, 1500, and 2000 μm/s and spin-coated at 2000 rpm (0.6 wt %). (e,f) Polarized Raman spectroscopy of TIPS-pentacene printed at 400 and 2000 μm/s (from 0° to 360° in steps of 30°). (g−l) GIWAXS measurements for the film printed at (g,h) 100, (i,j) 400, and (k,l) 1500 μm/s showing different morphologies. A schematic of lattice plane observed when the printing direction was aligned (m) parallel and (n) perpendicular to the incident beam direction. (o) Crystal orientation and the inferred printing direction in the $a-b$ plane.

(Figure 2m) to randomly oriented crystalline belts (Figure 2n,o). Especially, the crystalline belts obtained at 50 μm/s are generally continuous and extend from the beginning to the end

of the pattern, reaching a length scale of several centimeters that really longer than the direct spin coating[34] or comparable with align methods such as shearing.[35]
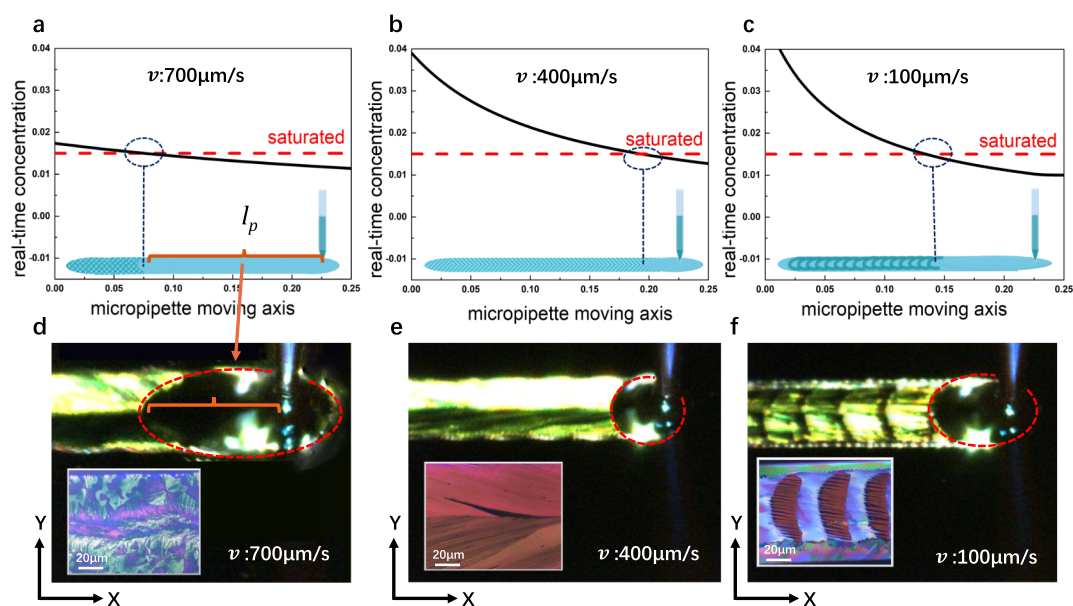
Figure 4. (a−c) Simulated curves of the concentration along the X-axis, with schemes of crystallizations. (d−f) Corresponding polarized optical images of TIPS-pentacene crystals printed at 700, 400, or 100 μm/s, 0.5 wt %. The insets are the crystals obtained after printing.

3.2. Anisotropic Properties. The anisotropic optical properties of printed TIPS-pentacene are studied using polarized UV−visible absorption spectroscopy at wavelengths in a range of 400−800 nm. All the crystalline films exhibit characteristic absorption peaks at 425, 450, 648, and 700 nm (Figure 3a−d), consistent with those of reported thin films.[36−38] Changes in the intensity of the absorption peaks are examined by rotating the samples by certain degrees with respect to the polarizer for the incident light (Figure 3a), where 0° is defined when the polarizer is parallel with the printing direction (Figure S5). The intensity is at the maximum at 30° and it reduces as the rotation angle increases and reaches a minimum at 90°, where the printed patterns are vertical to the polarized light. With further rotation of the sample, the intensity of the absorptions gradually recovers as the rotation degree reaches 120°. For the crystals printed at 1500 μm/s (Figure 3b), the maximum of absorption is obtained at 90° and a weaker dependence of the absorption on the rotation angle is observed. This is because crystals grow from the pattern edge toward the middle (vertical to the printing direction) because of the coffee ring effect[39−41] and surface tension.[42,43] For the crystals printed at 2000 μm/s (Figure 3c), the spherical crystals hardly exhibit a change in the absorption intensity due to the random crystalline orientation, comparable with a spin-coated film (Figure 3d).

Furthermore, angle-dependent polarized Raman spectroscopy is used to characterize the structural alignment of the polycrystalline thin films. When the polarized laser is parallel to the short (or long) axis along the side groups (or benzene rings), a maximum Raman scattering intensity will be observed at 1374 cm^{-1} (or 1578 cm^{-1}) signifying the short-axis (or long-axis) mode.[9] We take the peak of 1374 cm^{-1} to plot against angular variation (Figures 3e,f and S13). The crystalline belts printed at 400 μm/s exhibit large Raman scattering intensities at 150° and 330°, while the minimum intensities appear at 60° and 240°, exactly perpendicular to the former and corresponding to the long- and short-axis of the molecule, respectively. The strong scattering intensity indicates the stretching vibrations of C−C[44] and thus the orientation of the benzene

rings, as shown in Figure 3c. In contrast, very little anisotropy is found in the spherical crystalline film. Additionally, the randomly oriented crystallites are substantially smaller than the laser sport-size and lead to the very low anisotropy (Figure 3f). The GIWAXS measurements[38,39] were carried out with the printing direction of the samples aligned parallel and perpendicular to the incident beam (Figure 3g−l). It is revealed that (0kl) planes are mainly observed when the incident X-ray is perpendicular with the printing direction, whereas (h0l) planes are observed in the parallel alignment, which is consistent with previous observations of crystals deposited by jet printing.[45] In addition, the diffraction peaks for (210) planes are only observed when the incident beam is parallel to the printing direction, and the distance between (210) planes is approximate 3 Å, corresponding to the $\pi-\pi$ stacking distance. The results are consistent with other reports showing that TIPS-pentacene arranges into a lamellar packing structure with a 2D "brick-wall" motif.[46] Especially, when the orientations (210) with the strong $\pi-\pi$ interactions are generally along the channel, high charge transfer efficiency would be obtained as proved in previous studies.[47] Therefore, we would suggest that the printing direction is closed to the a-axis and probably between the a-axis and ⟨210⟩ direction, as shown in Figure 3o.

Among different printing speeds, 400 μm/s results in the highest crystallinity and the strongest orientational order, as suggested by the appearance of higher order diffraction peaks and relatively higher peak intensity. Observations of the intensity of absorptions, Raman spectroscopy, and GIWAXS confirm the anisotropy of guided crystallizations,[48−50] and such a highly ordered structure is supposed to benefit the device performance.[35,51,52]

3.3. Mechanism of Guided Crystallization. *3.3.1. Solution Dynamics.* The formation of diverse crystallization morphologies is essentially attributed to the concentration gradient generated during the meniscus-guided printing process.[53,54] In general, the printing speed determines the distance (l_p) from the pipette to the three-phase contact line, which is the boundary between the liquid-phase solution and
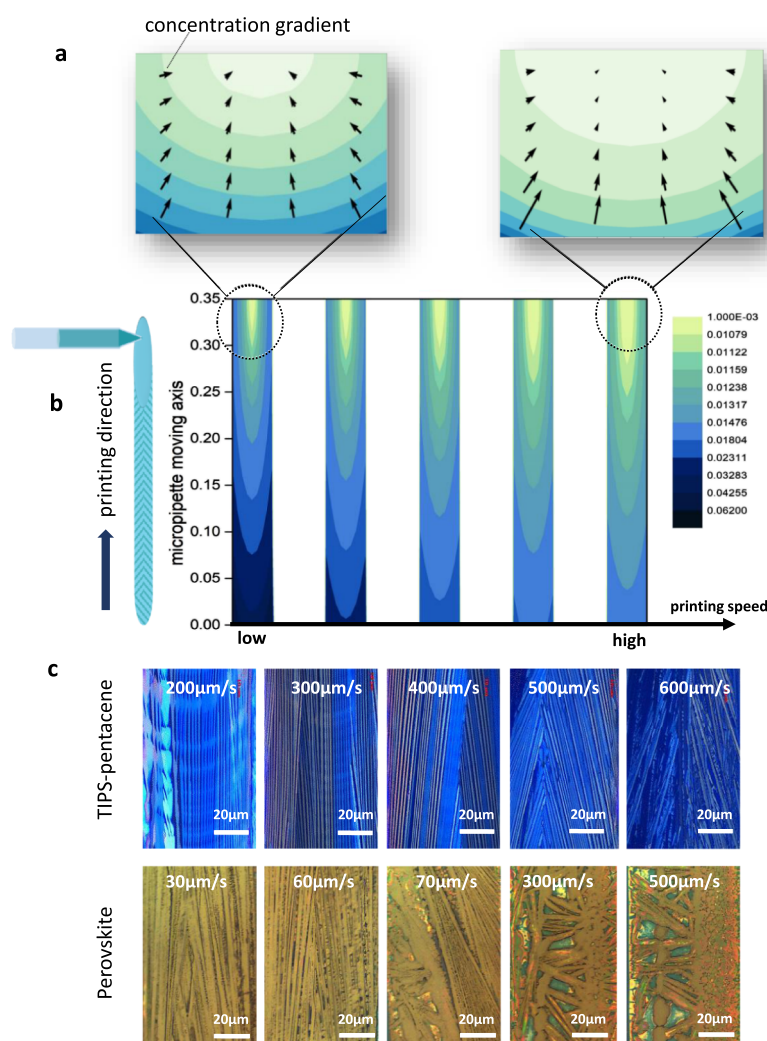
Figure 5. (a,b) Calculated concentration contours of the deposited solution on the substrate with printing speed of 200, 300, 400, 500, and 600 μm/s, respectively. (c) Images taken from the POM system for crystals of TIPS-pentacene formed by printing at 200−600 μm/s (upper) and crystals of perovskite MAPbI$_3$ formed by printing at 30−500 μm/s (below).

the solid-phase crystals. We found that l_p is influenced by printing speeds and it is closely related to the resulting crystal morphologies. A numerical model is proposed to help understand, with the X-axis (Y-axis) along (vertical to) the printing direction (Figure 4d). Along the X-axis and at a certain point (x_s), V (mL/s) is defined as the initial volume of the solution released from the micropipette onto the substrate in a unit area, with M as the initial mass of the solute (mg), r (mL/s) as the evaporation rate of the solution, and t (s) as the evaporation time of the solution. Then, the local concentration, C (mg/mL), is

$$C = M/(V - r \times t) \tag{1}$$

Constants include M and r, and variables include t and V. Note that t is determined by the distance between the position of micropipette (x_m) and the point x and the moving speed of the micropipette (v)

$$t = (x_m - x)/v \tag{2}$$

Moreover, the volume V increases with lowering of the printing speeds, because it takes longer time for the pipette to pass the area of a printed drop, which is D/v, and D is the diameter of the printed drops (constant, unit in millimeters).

In addition, we introduced a correction value V_{00} to define a non-zero V when the printing speed is high. Then, the semi-empirical description is

$$V = V_0 \times \frac{D}{v} + V_{00} \tag{3}$$

where V_0 and V_{00} are constants mainly determining the volume at low and high speeds, respectively, and their values are chosen according to the experimental results. At a certain time during printing, the local concentration can be drawn along the X-axis (black solid curves, Figure 4a−c). The dashed red line refers to the saturated concentration, and the intersection of two lines can roughly be regarded as the boundary between crystals and the liquid solution. The distance between the intersection and micropipette is considered to be l_p as mentioned above.

The calculated results are combined with the corresponding observations of solution dynamics and crystallization in Figure 4d−f. Three cases are considered according to the printing speed (v) that also corresponds to the different morphologies of crystallization. (1) At a high printing speed ($v = \sim$700 or >700 μm/s), the solution drags for a long-distance l_p until supersaturation occurs for crystallization. The evaporation
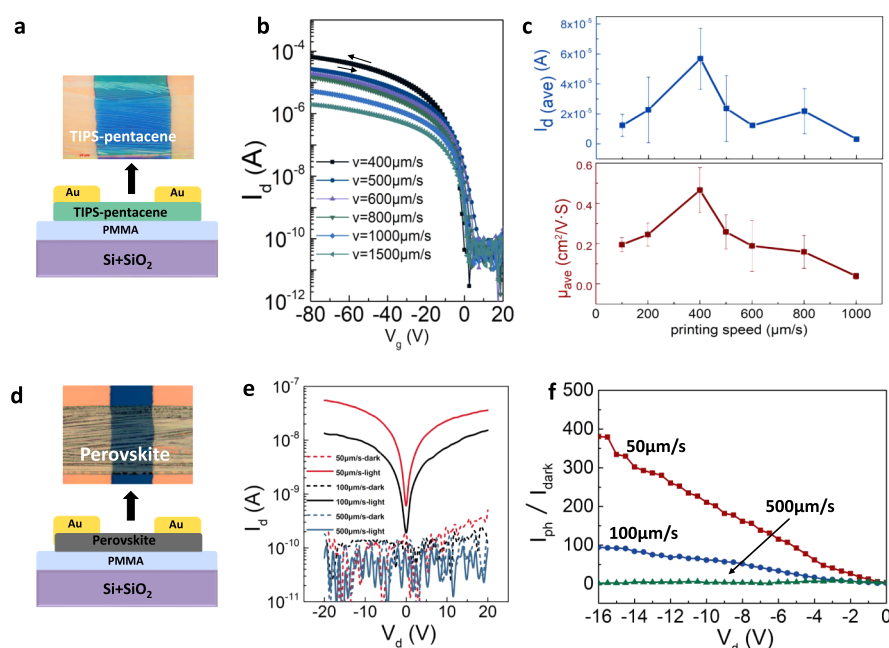
Figure 6. (a,d) Optical images of the channels of the TIPS-pentacene OTFT and MAPbI$_3$ photodetector. (b) Transfer characteristic curves of the OTFT. (c) Differential mobility and I_d ($V_g = -60$ V, $V_d = -40$ V) as a function of printing speed. (e) Photo-electric response currents of photodetectors using MAPbI$_3$ printed at different speeds. (f) Photo-to-dark current ratio of MAPbI$_3$ printed with different speeds.

cannot catch up with the moving micropipette, and thus, spontaneous crystallization occurs with the formation of a large number of nuclei and then spherical crystals,[55] such as those formed by spin-coating (Figure 4d). (2) At a medium printing speed ($v = \sim400$ μm/s), the distance l_p decreases, and as the TPC line recedes and well matches the evaporation rate, crystalline micro-arrays precipitate toward the concentration gradient and are thus locally aligned (known as the convective assembly[56]). This is slightly similar to that formed by dip-coating at a medium speed[57] (Figure 4e). (3) At a low speed ($v = \sim100$ μm/s), the distance l increases again because the solution volume (V) increases significantly and a severe coffee-ring effect (due to the evaporation rate at the liquid edge being faster than at the center) drags the solution.[58] Therefore, the concentration drops within l_p are relatively large, and as the solvent evaporates, slow, arc-shaped crystals with a lamellar structure grow along the moving direction of the micropipette, such as that formed near the edge of a film formed by drop-casting the solution[59,60] (Figure 4f). In general, a medium printing speed is needed to match the evaporation rate and to obtain oriented crystals of TIPS-pentacene,[61,62] and a relatively low local nuclei density results in crystallization without disturbance by neighboring crystals.

3.3.2. Formation of Crystalline Belts. We further analyze the aligned crystalline belts formed at the medium printing speed (from 200 to 600 μm/s) as below (Figure 5). The solution gradient along the Y-axis is also calculated by assuming a radial diffusion, and the 2D distribution of the concentration for different printing speeds within the same distance is shown in Figure 5a,b. The concentration increases from near the micropipette to far from it (Figure 5a). Contours are denser with larger gradients at a relatively low printing speed (~200 μm/s) and are accompanied by the more uniform direction of the crystals. At higher printing speeds (~600 μm/s), the contours are sparse, and the directions of the crystals begin to diversify[63] (Figure 5c TIPS-pentacene). In

Figure 5a, the arrows, which represent the direction and quantity of the gradient, point from the edge to the middle and along two directions that share a mirror plane. It corresponds well with the crystal growth along two directions and toward the middle (Figure 5c). In addition, the gradient contour near the micropipette is more uniform under slow moving speeds, while it becomes less uniform with higher printing speed (Figure 5a). The latter leads to less-ordered crystal growth for more formation of small crystallites (e.g. Figure 5c, TIPS-pentacene at 600 μm/s). Interestingly, a consistent trend from uniformly aligned to more diverse crystals is also found in depositing perovskite MAPbI$_3$ crystals, as shown in Figure 5c (perovskite). Generally, higher concentrations of the solution induce a higher density of nuclei and thicker films, as has been investigated in previous studies.[57] In this study, good matching between the gradient and evaporation rates has been obtained at 300–400 and 30–60 μm/s and leads to uniformly aligned crystals for TIPS-pentacene and MAPbI$_3$, respectively.

3.4. Electrical Performance of Devices. *3.4.1. Organic Transistor.* On the basis of the deposited crystals of TIPS-pentacene, TFTs are fabricated, as shown in Figure 6a. The OTFTs based on TIPS-pentacene are in the bottom-gate, top-contact configuration with SiO$_2$ as the gate insulator and Au as the source–drain electrodes. The transfer characteristics of OTFTs based on TIPS-pentacene deposited at various speeds (80–1500 μm/s) are investigated, as shown in Figure 6b. The on-current and field-effect mobility (μ) of these devices are shown in Figure 6c (more details are shown in Figure S10), which are extracted in the saturation regime from the slope[64] of the $\sqrt{I_d}$ versus V_g plot[65] using the equation: $\mu_{sat} = \frac{2L}{WC_i}\left(\frac{\partial \sqrt{I_d}}{\partial V_g}\right)^2$. Here, I_d is the drain current, V_g is the gate-voltage, L is the channel length (50 μm), W is the channel width (180–220 μm), and C_i is the capacitance per unit area (10.5 nF/cm^2). The optimized devices with aligned crystals (printed at 400 μm/s) exhibit the highest current and mobility
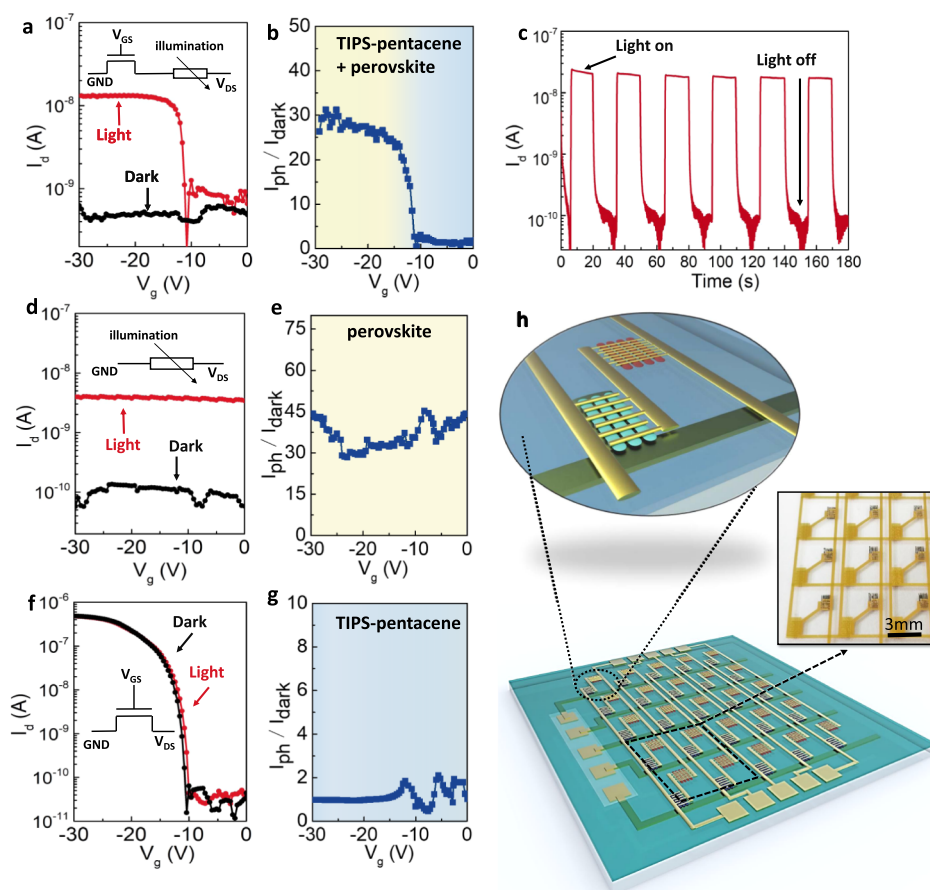
Figure 7. (a,d,f) Device structure and gate-tuning of current the OTFT, photodetector, and OTFT−photodetector cell measured under light or dark conditions (at $V_d = -1$ V). (b,e,g) Corresponding ratio of I_{ph}/I_{dark}. (c) Transient response of an OTFT−photodetector cell with periodic illumination. (h) Schematic representation of the active matrix of the OTFT−photodetector cell with an optical image.

value as compared with those with less ordered crystals deposited at either a higher or lower speed, in good agreement with the observations and analysis on crystal formation and anisotropy given above. The electronic performance of printed crystals is much better than the spherical crystals by spin coating, which exhibit larger threshold voltage and smaller channel current in devices (Figure S6 and Table S1).

In addition, the well-aligned crystals also exhibit obvious anisotropy in electrical performance. The on-current of the devices with the crystals along the channel (Figure S7f) is approximately 2 orders of magnitude higher than those with crystals vertical to the channel (Figure S7g,h) and the mobilities also attenuated obviously. Especially, when the electrodes gap the crystals with a mirror symmetry (Figure S7e), the devices show very low performance, attributed to the large resistance at the macroscopic grain boundaries that could be observed by optical microscope. The anisotropy in transistors can be well understood by referring the observations of crystal structures as discussed above. When the TIPS-pentacene are printed into well-aligned crystalline belts along the channel, the crystal direction[24] with strong $\pi-\pi$ interactions (revealed by the GIWAX and spectroscopy) is also mainly along the channel which highly assist the charge transport. Hence, we observed the best transistor performance when the printing is optimized (400 μm/s) to afford well-aligned crystals with minimum misalignment and grain boundaries along the channel.

3.4.2. Photodetector. The perovskite-based photodetectors are fabricated with a vacuum-deposited gold source and drain on the top of the perovskite MAPbI$_3$ film deposited under ambient conditions (Figure 6d). The devices are characterized under ambient conditions, and channel current is measured under illumination (white light) and in the dark. The photocurrent of perovskite MAPbI$_3$ photoconductors printed at different speeds are measured, as shown in Figure 6e, and the film printed at 500 μm/s shows insignificant photoresponse as the film is not continuous. The photoresponse for the piled, randomly oriented crystals produced at 500 μm/s is not observable, while the values for the continuous and aligned perovskite are above 300 times at the same voltage, indeed higher than the spin-coating methods,[66,67] indicating the crucial effect in improving device performance for coplanar photodetectors. It is worth to note that the films printed at speeds under 100 μm/s exhibit an apparent photocurrent of nearly 100 times higher than the film printed at 500 μm/s when biased at −15 V. The photo-to-dark current ratio (I_{ph}/I_{dark}) is presented in Figure 6f, which shows that the photocurrent of films printed at 50 and 100 μm/s increases linearly with drain voltage.

3.4.3. Active Photodetector. As shown above, the OTFTs exhibit a strong gate-tuning effect, while the photodetectors exhibit a clear photoresponse. Notice that the OTFTs exhibit a negligible photoresponse (Figure 7f,g), and the perovskite photodetectors do not show gate-tunability with a constant current in air (Figure 7d,e). However, the active matrix of a
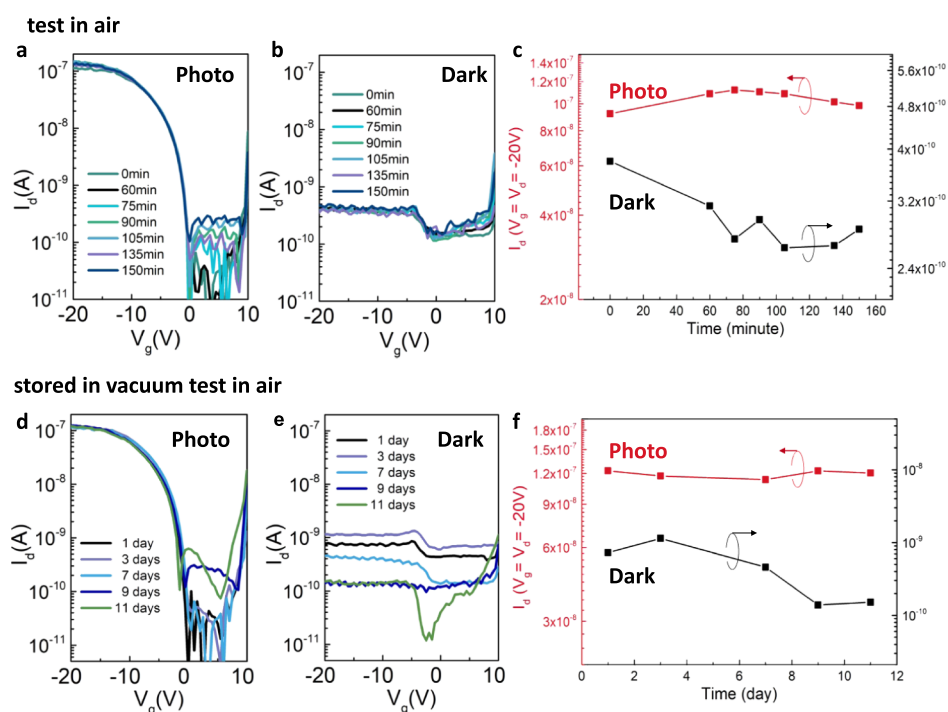
Figure 8. (a,b) Photocurrent and dark current of a TFT−photodetector (TIPS-perovskite) unit during continuous measurement for 150 min in atmosphere conditions. (c) Corresponding photocurrent and dark current at bias with $V_g = -20$ V and $V_d = -20$ V. (d,e) Evolution of photocurrents of a TFT−photodetector (TIPS-perovskite) unit stored in vacuum for 12 days. (f) Corresponding photocurrent and dark current at bias with $V_g = -20$ V and $V_d = -20$ V.

photodetector calls for a stable off-state at zero gate−bias to maintain low power consumption. Therefore, we combine the advantages of the two devices to make gate-tunable or electrical-switchable photodetectors. The characteristics of an individual photodetecting cell is shown in Figure 7a,b, where a perovskite photodetector is connected to the drain electrode of a TIPS-pentacene OTFT. The device is scanned by sweeping the gate voltage and setting the source−drain voltage as $V_d = -1$ V. Without gate biasing, the detecting cell is not conductive even with illumination because of the low conductivity of the OTFT. At gate voltages larger than the threshold and with illumination, the conductivity of both the OTFT and photodetector sharply increases. Therefore, the device remains off to maintain low power consumption until when there are simultaneously light and a proper gate−bias. The transient response of the detector cell is measured by periodic illumination (Figure 7c) and shows a stable response to light switching. Because of the small W/L and ambient fabrication conditions, the light-to-dark current ratio is limited to approximately 100, which can be further enhanced by optimizing the fabrication and using a larger W/L ratio.

In addition, we tested the stability of the active photodetectors in ambient conditions with humidity lower than 40%. First, an individual perovskite photodetector (a resistor) was measured under continuous bias conditions. The evolution of the photocurrent and dark current at $V_d = -20$ V is recorded in Figure S14. The device covered with CYTOP exhibits slightly lager photo-current as compared with the one without passivation. Even though, the photodetector without encapsulation exhibited a stable performance during the continuous measurement for 600 s. Second, we measured the OTFT−photodetector unit for several times during 150 min (Figure 8a,b). The evolution of the photocurrent and dark-current in

the on-state ($V_d = -20$ V, $V_g = -20$ V) was measured at different time (Figure 8c). The photocurrents slightly changed within 2.0×10^{-8} A and the dark-current has negligible variations within 1.2×10^{-10} A, indicating that we could obtain stable devices in the short-term and continuous measurements. Finally, we kept devices in a vacuum cabinet for 11 days and took out to test them in air for several times. The photocurrent and dark current are shown in Figure 8d,e. Photocurrents changed within 9.8×10^{-9} A and the dark current slightly decreased 1.1×10^{-9} A (Figure 8f).

4. CONCLUSIONS

The guided crystallization of organic and perovskite semiconductors has been achieved by printing solutions with the ultrasonicated dispenser. From slow to high moving speeds, the dispenser generates platelike crystals, aligned crystalline belts, and spherical crystals. The crystallization is closely related to the concentration gradient profile of the liquid area from the solid crystals to the dispenser. Highly ordered, aligned TIPS-pentacene and perovskite MAPbI$_3$ semiconductors have been obtained using an optimized moving speed of the dispenser. The materials exhibit strong anisotropy in UV−vis absorption and Raman scattering spectroscopy analyses, with the intensities corresponding well to the orientation of the crystals. The TFT and photodetector devices utilizing aligned crystals exhibit higher on-currents than those devices with disordered crystals, which can be understood by the reduction of crystal boundaries and the transport along the π−π stacking. Finally, we combine the two types of devices and demonstrate an OTFT-controlled photodetector for visible-light sensing. The detector cell switches from the off-state to the on-state only with both illumination and gate-tuning and works well under ambient conditions. The presented studies demonstrate

the potential of using the ultrasonicated dispenser to print electronic and opto-electronic devices.

ASSOCIATED CONTENT

Ⓢ Supporting Information

The Supporting Information is available free of charge on the ACS Publications website at DOI: 10.1021/acsami.8b10861.

> Details of crystals obtained under various conditions (images of the dynamics for ultrasonic printing process, different concentrations, printing speeds, or substrate treatments); schematic of sample position and polarization direction during UV−visible absorption; transfer curves with hysteresis under different printing speeds; polarized POM images and Raman intensity of the crystals; schematic diagram showing the lattice constant; and tabulated comparison of observed parameters and estimation of dispensing rate and related parameters (PDF)
>
> Recording during printing at different printing velocities (MPG)

AUTHOR INFORMATION

Corresponding Author
*E-mail: liuchuan5@mail.sysu.edu.cn.

ORCID Ⓓ
Chenning Liu: 0000-0003-4298-7416
Fuhua Dai: 0000-0002-3421-4416
Xinhui Lu: 0000-0002-1908-3294
Xuying Liu: 0000-0001-9190-4651

Author Contributions
[⊥]C.L. and H.Z. contribute equally to this work.

Notes
The authors declare no competing financial interest.

ACKNOWLEDGMENTS

REFERENCES

(1) Tang, W.; Feng, L.; Zhao, J.; Cui, Q.; Chen, S.; Guo, X. Inkjet Printed Fine Silver Electrodes For All-Solution-Processed Low-Voltage Organic Thin Film Transistors. *J. Mater. Chem. C* **2014**, *2*, 1995.

(2) Brossard, F. S. F.; Pecunia, V.; Ramsay, A. J.; Griffiths, J. P.; Hugues, M.; Sirringhaus, H. Inkjet-Printed Nanocavities on a Photonic Crystal Template. *Adv. Mater.* **2017**, *29*, 1704425.

(3) Schnitker, J.; Adly, N.; Seyock, S.; Bachmann, B.; Yakushenko, A.; Wolfrum, B.; Offenhäusser, A. Rapid Prototyping of Ultralow-Cost, Inkjet-Printed Carbon Microelectrodes for Flexible Bioelectronic Devices. *Adv. Biosyst.* **2018**, *2*, 1700136.

(4) Li, L.; Pan, L.; Ma, Z.; Yan, K.; Cheng, W.; Shi, Y.; Yu, G. All Inkjet-Printed Amperometric Multiplexed Biosensors Based on Nanostructured Conductive Hydrogel Electrodes. *Nano Lett.* **2018**, *18*, 3322−3327.

(5) Liu, T.; Zhao, J.; Xu, W.; Dou, J.; Zhao, X.; Deng, W.; Wei, C.; Xu, W.; Guo, W.; Su, W.; Jie, J.; Cui, Z. Flexible Integrated Diode-Transistor Logic (DTL) Driving Circuits Based on Printed Carbon Nanotube Thin Film Transistors with Low Operation Voltage. *Nanoscale* **2018**, *10*, 614−622.

(6) Cai, L.; Zhang, S.; Zhang, Y.; Li, J.; Miao, J.; Wang, Q.; Yu, Z.; Wang, C. Direct Printing for Additive Patterning of Silver Nanowires for Stretchable Sensor and Display Applications. *Adv. Mater. Technol.* **2018**, *3*, 1700232.

(7) Minemawari, H.; Yamada, T.; Matsui, H.; Tsutsumi, J.; Haas, S.; Chiba, R.; Kumai, R.; Hasegawa, T. Inkjet Printing of Single-Crystal Films. *Nature* **2011**, *475*, 364−367.

(8) Mei, Y.; Loth, M. A.; Payne, M.; Zhang, W.; Smith, J.; Day, C. S.; Parkin, S. R.; Heeney, M.; McCulloch, I.; Anthopoulos, T. D.; Anthony, J. E.; Jurchescu, O. D. High Mobility Field-Effect Transistors with Versatile Processing from a Small-Molecule Organic Semiconductor. *Adv. Mater.* **2013**, *25*, 4352−4357.

(9) Rigas, G.-P.; Payne, M. M.; Anthony, J. E.; Horton, P. N.; Castro, F. A.; Shkunov, M. Spray Printing of Organic Semiconducting Single Crystals. *Nat. Commun.* **2016**, *7*, 13531.

(10) Kim, D.; Jeong, S.; Lee, S.; Park, B. K.; Moon, J. Organic Thin Film Transistor Using Silver Electrodes by the Ink-Jet Printing Technology. *Thin Solid Films* **2007**, *515*, 7692−7696.

(11) de Gans, B.-J.; Kazancioglu, E.; Meyer, W.; Schubert, U. S. Inkjet Printing Polymers and Polymer Libraries Using Micropipettes. *Macromol. Rapid Commun.* **2004**, *25*, 292−296.

(12) Park, B. K.; Kim, D.; Jeong, S.; Moon, J.; Kim, J. S. Direct Writing of Copper Conductive Patterns by Ink-Jet Printing. *Thin Solid Films* **2007**, *515*, 7706−7711.

(13) Jang, D.; Kim, D.; Moon, J. Influence of Fluid Physical Properties on Ink-Jet Printability. *Langmuir* **2009**, *25*, 2629−2635.

(14) Park, J.-U.; Hardy, M.; Kang, S. J.; Barton, K.; Adair, K.; Mukhopadhyay, D. k.; Lee, C. Y.; Strano, M. S.; Alleyne, A. G.; Georgiadis, J. G.; Ferreira, P. M.; Rogers, J. A. High-Resolution Electrohydrodynamic Jet Printing. *Nat. Mater.* **2007**, *6*, 782−789.

(15) Paulus, F.; Engelhart, J. U.; Hopkinson, P. E.; Schimpf, C.; Leineweber, A.; Sirringhaus, H.; Vaynzof, Y.; Bunz, U. H. F. The Effect of Tuning the Microstructure of TIPS-Tetraazapentacene on The Performance of Solution Processed Thin Film Transistors. *J. Mater. Chem. C* **2016**, *4*, 1194−1200.

(16) Deng, W.; Zhang, X.; Huang, L.; Xu, X.; Wang, L.; Wang, J.; Shang, Q.; Lee, S.-T.; Jie, J. Aligned Single-Crystalline Perovskite Microwire Arrays for High-Performance Flexible Image Sensors with Long-Term Stability. *Adv. Mater.* **2016**, *28*, 2201−2208.

(17) Yu, X.; Zhou, N.; Han, S.; Lin, H.; Buchholz, D. B.; Yu, J.; Chang, R. P. H.; Marks, T. J.; Facchetti, A. Flexible Spray-Coated TIPS-pentacene Organic Thin-Film Transistors as Ammonia Gas Sensors. *J. Mater. Chem. C* **2013**, *1*, 6532−6535.

(18) Paterson, A. F.; Treat, N. D.; Zhang, W.; Fei, Z.; Wyatt-Moon, G.; Faber, H.; Vourlias, G.; Patsalas, P. A.; Solomeshch, O.; Tessler, N.; Heeney, M.; Anthopoulos, T. D. Small Molecule/Polymer Blend Organic Transistors with Hole Mobility Exceeding 13 cm V^{-1}s^{-1}. *Adv. Mater.* **2016**, *28*, 7791−7798.

(19) Park, J. H.; Lee, K. H.; Mun, S.-j.; Ko, G.; Heo, S. J.; Kim, J. H.; Kim, E.; Im, S. Self-assembly of Organic Channel/Polymer Dielectric Layer in Solution Process for Low-Voltage Thin-Film Transistors. *Org. Electron.* **2010**, *11*, 1688−1692.

(20) Pitsalidis, C.; Kalfagiannis, N.; Hastas, N. A.; Karagiannidis, P. G.; Kapnopoulos, C.; Ioakeimidis, A.; Logothetidis, S. High Performance Transistors Based on the Controlled Growth of Triisopropylsilylethynyl-pentacene Crystals via Non-Isotropic Solvent Evaporation. *RSC Adv.* **2014**, *4*, 20804−20813.

(21) Wade, J.; Steiner, F.; Niedzialek, D.; James, D. T.; Jung, Y.; Yun, D.-J.; Bradley, D. D. C.; Nelson, J.; Kim, J.-S. Charge Mobility Anisotropy of Functionalized Pentacenes in Organic Field Effect Transistors Fabricated by Solution Processing. *J. Mater. Chem. C* **2014**, *2*, 10110−10115.

(22) Giri, G.; Park, S.; Vosgueritchian, M.; Shulaker, M. M.; Bao, Z. High-Mobility, Aligned Crystalline Domains of TIPS-Pentacene with

Metastable Polymorphs Through Lateral Confinement of Crystal Growth. *Adv. Mater.* **2014**, *26*, 487−493.

(23) Yang, T.; Mehta, J. S.; Haruk, A. M.; Mativetsky, J. M. Targeted Deposition of Organic Semiconductor Stripes onto Rigid, Flexible, and Three-Dimensional Substrates. *J. Mater. Chem. C* **2018**, *6*, 2970−2977.

(24) Li, H.; Tee, B. C.-K.; Cha, J. J.; Cui, Y.; Chung, J. W.; Lee, S. Y.; Bao, Z. High-Mobility Field-Effect Transistors from Large-Area Solution-Grown Aligned C60 Single Crystals. *J. Am. Chem. Soc.* **2012**, *134*, 2760−2765.

(25) Scriven, L. E. Physics and Applications of DIP Coating and Spin Coating. *MRS Proceedings*; Cambridge University Press, 1988; Vol. *121*, p 717.

(26) Brutin, D.; Starov, V. Recent advances in Droplet Wetting and Evaporation. *Chem. Soc. Rev.* **2018**, *47*, 558−585.

(27) Li, L.; Gao, P.; Wang, W.; Müllen, K.; Fuchs, H.; Chi, L. Growth of Ultrathin Organic Semiconductor Microstripes with Thickness Control in the Monolayer Precision. *Angew. Chem., Int. Ed.* **2013**, *52*, 12530−12535.

(28) Peng, B.; Huang, S.; Zhou, Z.; Chan, P. K. L. Solution-Processed Monolayer Organic Crystals for High-Performance Field-Effect Transistors and Ultrasensitive Gas Sensors. *Adv. Funct. Mater.* **2017**, *27*, 1700999.

(29) Cheng, H.-L.; Mai, Y.-S.; Chou, W.-Y.; Chang, L.-R.; Liang, X.-W. Thickness-Dependent Structural Evolutions and Growth Models in Relation to Carrier Transport Properties in Polycrystalline Pentacene Thin Films. *Adv. Funct. Mater.* **2007**, *17*, 3639−3649.

(30) Riera-Galindo, S.; Tamayo, A.; Mas-Torrent, M. Role of Polymorphism and Thin-Film Morphology in Organic Semiconductors Processed by Solution Shearing. *ACS Omega* **2018**, *3*, 2329−2339.

(31) Tseng, H.-R.; Phan, H.; Luo, C.; Wang, M.; Perez, L. A.; Patel, S. N.; Ying, L.; Kramer, E. J.; Nguyen, T.-Q.; Bazan, G. C.; Heeger, A. J. High-Mobility Field-Effect Transistors Fabricated with Macroscopic Aligned Semiconducting Polymers. *Adv. Mater.* **2014**, *26*, 2993−2998.

(32) Zhao, K.; Khan, H. U.; Li, R.; Su, Y.; Amassian, A. Entanglement of Conjugated Polymer Chains Influences Molecular Self-Assembly and Carrier Transport. *Adv. Funct. Mater.* **2013**, *23*, 6024−6035.

(33) Koch, F. P. V.; Rivnay, J.; Foster, S.; Müller, C.; Downing, J. M.; Buchaca-Domingo, E.; Westacott, P.; Yu, L.; Yuan, M.; Baklar, M.; Fei, Z.; Luscombe, C.; McLachlan, M. A.; Heeney, M.; Rumbles, G.; Silva, C.; Salleo, A.; Nelson, J.; Smith, P.; Stingelin, N. The Impact of Molecular Weight on Microstructure and Charge Transport in Semicrystalline Polymer Semiconductors−poly(3-hexylthiophene), a Model Study. *Prog. Polym. Sci.* **2013**, *38*, 1978−1989.

(34) Ji, L.; Hsu, H.-Y.; Lee, J. C.; Bard, A. J.; Yu, E. T. High-Performance Photodetectors Based on Solution-Processed Epitaxial Grown Hybrid Halide Perovskites. *Nano Lett.* **2018**, *18*, 994−1000.

(35) Deng, W.; Zhang, X.; Huang, L.; Xu, X.; Wang, L.; Wang, J.; Shang, Q.; Lee, S.-T.; Jie, J. Aligned Single-Crystalline Perovskite Microwire Arrays for High-Performance Flexible Image Sensors with Long-Term Stability. *Adv. Mater.* **2016**, *28*, 2201−2208.

(36) Martins, C. S. G. Optimization of Printed TIPS-Pentacene Thin-Film Applied on OFET technology. Master Thesis, University of São Paulo, São Paulo, Brazil, 2016, p 61.

(37) James, D. T.; Frost, J. M.; Wade, J.; Nelson, J.; Kim, J.-S. Controlling Microstructure of Pentacene Derivatives by Solution Processing: Impact of Structural Anisotropy on Optoelectronic Properties. *ACS Nano* **2013**, *7*, 7983−7991.

(38) Li, Y.; Wu, Y.; Liu, P.; Prostran, Z.; Gardner, S.; Ong, B. S. Stable Solution-Processed High-Mobility Substituted Pentacene Semiconductors. *Chem. Mater.* **2007**, *19*, 418−423.

(39) Deegan, R. D.; Bakajin, O.; Dupont, T. F.; Huber, G.; Nagel, S. R.; Witten, T. A. Capillary Flow as the Cause of Ring Stains from Dried Liquid Drops. *Nature* **1997**, *389*, 827−829.

(40) Yu, L.; Niazi, M. R.; Ndjawa, G. O. N.; Li, R.; Kirmani, A. R.; Munir, R.; Balawi, A. H.; Laquai, F.; Amassian, A. Programmable and Coherent Crystallization of Semiconductors. *Sci. Adv.* **2017**, *3*, No. e1602462.

(41) Liu, C.; Liu, X.; Xu, Y.; Sun, H.; Li, Y.; Shi, Y.; Lee, M. V.; Yamada, T.; Hasegawa, T.; Noh, Y.-Y.; Minari, T. Generating One-Dimensional Micro- or Nano-Structures with In-Plane Alignment by Vapor-Driven Wetting Kinetics. *Mater. Horiz.* **2017**, *4*, 259.

(42) Schwabe, D.; Scharmann, A.; Preisser, F.; Oeder, R. Experiments on Surface Tension Driven Flow in Floating Zone Melting. *J. Cryst. Growth* **1978**, *43*, 305−312.

(43) Zhumekenov, A. A.; Burlakov, V. M.; Saidaminov, M. I.; Alofi, A.; Haque, M. A.; Turedi, B.; Davaasuren, B.; Dursun, I.; Cho, N.; El-Zohry, A. M.; De Bastiani, M.; Giugni, A.; Torre, B.; Di Fabrizio, E.; Mohammed, O. F.; Rothenberger, A.; Wu, T.; Goriely, A.; Bakr, O. M. The Role of Surface Tension in the Crystallization of Metal Halide Perovskites. *ACS Energy Lett.* **2017**, *2*, 1782−1788.

(44) James, D. T.; Kjellander, B. K. C.; Smaal, W. T. T.; Gelinck, G. H.; Combe, C.; McCulloch, I.; Wilson, R.; Burroughes, J. H.; Bradley, D. D. C.; Kim, J.-S. Thin-Film Morphology of Inkjet-Printed Single-Droplet Organic Transistors Using Polarized Raman Spectroscopy: Effect of Blending TIPS-Pentacene with Insulating Polymer. *ACS Nano* **2011**, *5*, 9824−9835.

(45) Kim, K.; Bae, J.; Noh, S. H.; Jang, J.; Kim, S. H.; Park, C. E. Direct Writing and Aligning of Small-Molecule Organic Semiconductor Crystals via "Dragging Mode" Electrohydrodynamic Jet Printing for Flexible Organic Field-Effect Transistor Arrays. *J. Phys. Chem. Lett.* **2017**, *8*, 5492−5500.

(46) James, D. T.; Frost, J. M.; Wade, J.; Nelson, J.; Kim, J.-S. Controlling Microstructure of Pentacene Derivatives by Solution Processing: Impact of Structural Anisotropy on Optoelectronic Properties. *ACS Nano* **2013**, *7*, 7983−7991.

(47) Chen, J.; Tee, C. K.; Shtein, M.; Martin, D. C.; Anthony, J. Controlled Solution Deposition and Systematic Study of Charge-Transport Anisotropy in Single Crystal and Single-Crystal Textured TIPS Pentacene Thin Films. *Org. Electron.* **2009**, *10*, 696−703.

(48) Chen, L.; Zhao, K.; Chi, S.; Liu, J.; Yu, X.; Han, Y. Improving Fiber Alignment by Increasing the Planar Conformation of Isoindigo-based Conjugated Polymers. *Mater. Chem. Front.* **2017**, *1*, 286−293.

(49) Lin, Z.; Guo, X.; Zhou, L.; Zhang, C.; Chang, J.; Wu, J.; Zhang, J. Solution-Processed High Performance Organic Thin Film Transistors Enabled by Roll-to-roll Slot Die Coating Technique. *Org. Electron.* **2018**, *54*, 80−88.

(50) Abdullah, I.; Lan, H.; Morrison, J.; Alharbi, A.; Macdonald, J. E.; Yeates, S. G. The Synergistic Role of Azeotropic Solvent Mixtures and Atactic Polystyrene on the Morphology, Crystallization and Field Effect Mobility of Thin Film 6,13-bis(triisopropylsilylethynyl)-pentacene based Semiconductors. *J. Mater. Sci.: Mater. Electron.* **2018**, *29*, 9804.

(51) Xu, X.; Yao, Y.; Shan, B.; Gu, X.; Liu, D.; Liu, J.; Xu, J.; Zhao, N.; Hu, W.; Miao, Q. Electron Mobility Exceeding 10 cm ^{2} V $^{-1}$ s $^{-1}$ and Band-Like Charge Transport in Solution-Processed n-Channel Organic Thin-Film Transistors. *Adv. Mater.* **2016**, *28*, 5276−5283.

(52) Yang, S.; Park, S.; Bintinger, J.; Bonnassieux, Y.; Anthony, J.; Kymissis, I. Employing Pneumatic Nozzle Printing for Controlling the Crystal Growth of Small Molecule Organic Semiconductor for Field-Effect Transistors. *Adv. Electron. Mater.* **2018**, *4*, 1700534.

(53) Gu, X.; Shaw, L.; Gu, K.; Toney, M. F.; Bao, Z. The Meniscus-Guided Deposition of Semiconducting Polymers. *Nat. Commun.* **2018**, *9*, 534.

(54) Su, Y.; Gao, X.; Liu, J.; Xing, R.; Han, Y. Uniaxial Alignment of Triisopropylsilylethynyl Pentacene via Zone-Casting Technique. *Phys. Chem. Chem. Phys.* **2013**, *15*, 14396.

(55) Giri, G.; Verploegen, E.; Mannsfeld, S. C. B.; Atahan-Evrenk, S.; Kim, D. H.; Lee, S. Y.; Becerril, H. A.; Aspuru-Guzik, A.; Toney, M. F.; Bao, Z. Tuning Charge Transport in Solution-Sheared Organic Semiconductors Using Lattice Strain. *Nature* **2011**, *480*, 504−508.

(56) Fleck, N. A.; McMeeking, R. M.; Kraus, T. Convective Assembly of a Particle Monolayer. *Langmuir* **2015**, *31*, 13655−13663.

(57) Li, L.; Gao, P.; Wang, W.; Müllen, K.; Fuchs, H.; Chi, L. Growth of Ultrathin Organic Semiconductor Microstripes with

Thickness Control in the Monolayer Precision. *Angew. Chem., Int. Ed.* **2013**, *52*, 12530−12535.

(58) Vladimirov, I.; Kellermeier, M.; Geßner, T.; Molla, Z.; Grigorian, S.; Pietsch, U.; Schaffroth, L. S.; Kühn, M.; May, F.; Weitz, R. T. High-Mobility, Ultrathin Organic Semiconducting Films Realized by Surface-Mediated Crystallization. *Nano Lett.* **2018**, *18*, 9−14.

(59) Kwak, D.; Lim, J. A.; Kang, B.; Lee, W. H.; Cho, K. Self-Organization of Inkjet-Printed Organic Semiconductor Films Prepared in Inkjet-Etched Microwells. *Adv. Funct. Mater.* **2013**, *23*, 5224−5231.

(60) Eslamian, M.; Soltani-Kordshuli, F. Development of Multiple-Droplet Drop-Casting Method for the Fabrication of Coatings and Thin Solid Films. *J. Coat. Technol. Res.* **2018**, *15*, 271−280.

(61) Xiao, C.; Kan, X.; Liu, C.; Jiang, W.; Zhao, G.; Zhao, Q.; Zhang, L.; Hu, W.; Wang, Z.; Jiang, L. Controlled Formation of Large-Area Single-Crystalline TIPS-pentacene Arrays Through Super-hydrophobic Micropillar Flow-Coating. *J. Mater. Chem. C* **2017**, *5*, 2702−2707.

(62) Chang, J.; Chi, C.; Zhang, J.; Wu, J. Controlled Growth of Large-Area High-Performance Small-Molecule Organic Single-Crystalline Transistors by Slot-Die Coating Using A Mixed Solvent System. *Adv. Mater.* **2013**, *25*, 6442−6447.

(63) Wade, J.; Steiner, F.; Niedzialek, D.; James, D. T.; Jung, Y.; Yun, D.-J.; Bradley, D. D. C.; Nelson, J.; Kim, J.-S. Charge Mobility Anisotropy of Functionalized Pentacenes in Organic Field Effect Transistors Fabricated by Solution Processing. *J. Mater. Chem. C* **2014**, *2*, 10110−10115.

(64) Liu, C.; Li, G.; Di Pietro, R.; Huang, J.; Noh, Y.-Y.; Liu, X.; Minari, T. Device Physics of Contact Issues for the Overestimation and Underestimation of Carrier Mobility in Field-Effect Transistors. *Phys. Rev. Appl.* **2017**, *8*, 034020.

(65) Liu, C.; Huang, K.; Park, W.-T.; Li, M.; Yang, T.; Liu, X.; Liang, L.; Minari, T.; Noh, Y.-Y. A Unified Understanding of Charge Transport in Organic Semiconductors: the Importance of Attenuated Delocalization for the Carriers. *Mater. Horiz.* **2017**, *4*, 608.

(66) Shao, Y.; Fang, Y.; Li, T.; Wang, Q.; Dong, Q.; Deng, Y.; Yuan, Y.; Wei, H.; Wang, M.; Gruverman, A.; Shield, J.; Huang, J. Grain Boundary Dominated Ion Migration in Polycrystalline Organic−Inorganic Halide Perovskite Films. *Energy Environ. Sci.* **2016**, *9*, 1752−1759.

(67) Chen, P.; Bai, Y.; Wang, S.; Lyu, M.; Yun, J.-H.; Wang, L. In Situ Growth of 2D Perovskite Capping Layer for Stable and Efficient Perovskite Solar Cells. *Adv. Funct. Mater.* **2018**, *28*, 1706923.